Delft University of Technology

Analyzing efficacy and safety of anti-fungal blue light therapy via kernel-based modeling the reactive oxygen species induced by light

Wang, Tianfeng; Dong, Jianfei; Zhang, Guoqi

DOI

Publication date
2022

Document Version
Final published version

Published in
IEEE Transactions on Biomedical Engineering

Important note
To cite this publication, please use the final published version (if applicable).
Please check the document version above.

Analyzing Efficacy and Safety of Anti-Fungal Blue Light Therapy via Kernel-Based Modeling the Reactive Oxygen Species Induced by Light

Tianfeng Wang [iD], Jianfei Dong [iD], and Guoqi Zhang, *Fellow, IEEE*

Abstract—*Objective:* The goal of this study is to investigate the efficacy, safety, and mechanism of ABL for inactivating *Candida albicans* (*C. albicans*), and to determine the best wavelength for treating candida infected disease, by experimental measurements and dynamic modeling. *Methods:* The changes in reactive oxygen species (ROS) in *C. albicans* and human host cells under the irradiation of 385, 405, and 415 nm wavelengths light with irradiance of 50 mW/cm^2 were measured. Moreover, a kernel-based nonlinear dynamic model, i.e., nonlinear autoregressive with exogenous inputs (NARX), was developed and applied to predict the concentration of light-induced ROS, whose kernels were selected by a newly developed algorithm based on particle swarm optimization (PSO). *Results:* The ROS concentration was increased respectively about 10-12 times in *C. albicans* and about 3-6 times in human epithelial cells by the ABL treatment with the same fluence of 90 J/cm^2. The NARX models were respectively fitted to the data from the experiments on both types of cells. Besides, four different kernel functions, including Gaussian, Laplace, linear and polynomial kernels, were compared in their fitting accuracies. The errors with the Laplace kernel turned out to be only 0.2704 and 0.0593, as respectively fitted to the experimental data of the *C. albicans* and human host cells. *Conclusion:* The results demonstrated the effectiveness of the NARX modeling approach, and revealed that the 415 nm light was more effective as an anti-fungal treatment with less damage to the host cells than the 405 or 385 nm light. *Significance:* The kernel-based NARX model identification algorithm offers opportunities for determining the effective and safe light dosages in treating various fungal infection diseases.

Index Terms—Anti-fungal blue light therapy, Kernel selection, NARX modeling, nonlinear dynamics, reactive oxygen species.

Tianfeng Wang is with the Suzhou Institute of Biomedical Engineering and Technology, Chinese Academy of Sciences, China, and also with the Department of Microelectronics, Delft University of Technology, The Netherlands.

Jianfei Dong is with the Suzhou Institute of Biomedical Engineering and Technology, Chinese Academy of Sciences, Suzhou 215163, China (e-mail: jfeidong@hotmail.com).

Guoqi Zhang is with the Department of Microelectronics, Delft University of Technology, The Netherlands.

I. INTRODUCTION

CANDIDA *albicans* (*C. albicans*) is widely found in nature and commonly occurs as a superficial infection on mucous membranes, such as the mouth, throat, gut, and vagina [1]–[3], and is the most common fungal pathogen of humans [4]. *Candida* species are naturally found in 10%-20% of women [5]; and 75% of women have at least one episode of vulvovaginal candidiasis (VVC) [6]. About 90% of the overall cases of VVC are caused by *C. albicans* [7]. Topical antimycotic drugs and more convenient oral azole agents are the main treatments for VVC [2]. However, *C. albicans* has shown increased resistance to these drugs [8], [9]. Therefore it is crucial to identify new ways to treat fungal infections. Photodynamic therapy (PDT) has been investigated as an alternative to treat localized infectious diseases due to the rapid action and avoidance of drug resistance by these pathogens [10]. Similar to PDT, anti-fungal blue light (ABL) therapy relies only on endogenous photosensitizers (PS) of the pathogens, and are hence safer to use.

The hypothesized mechanism of the antimicrobial effect of PDT and ABL is that light photons excite either exogenous PS in the former case or endogenous PS in the latter, which, in turn, produces highly toxic ROS in cells [11]. Due to the type and content of endogenous PS in different cells, their susceptibility to ABL can also be different. Fungal PS content is normally higher than that of human cells. Thus, fungi are more susceptible to ABL and, hence, ABL has been widely investigated for treating fungal infections. For instance, the inactivation rate of *C. albicans* by ABL was 42-fold faster than human keratinocytes [12]. A dynamic model was developed based on the viability of *C. albicans* and vaginal epithelial (V. E.) cells during ABL irradiation, which demonstrated that the shorter ABL wavelength around 410 nm achieved a higher anti-fungal effect than 450 nm [13]. The safety of ABL in treating candidal vaginitis was investigated in [14], which found that the blue light at 405 nm preferentially induced more death to the pathogenic cells than to the human V.E. cells. Furthermore, no genotoxicity of blue light to the V. E. cells was observed at the dosage for inactivating the pathogen. However, to the best of our knowledge, no study has focused on the ROS concentrations in fungi and host cells for treating VVC, i.e., *C. albicans* and the V. E. cells.

Some first-principle models have been proposed based on the PDT mechanism. For instance, modeling of the dynamic

changes in ROS concentrations has been well investigated [15]–[17], which are highly nonlinear models. These first-principle models precisely fit the dynamic changes in ROS concentrations. However, a dynamic model for the ROS concentrations to treat fungal infections has not been established. This can be attributed to the difficulty of using a first principle model, i.e., the parameters are related to the PS characteristics, which are determined experimentally. For instance, up to 21 parameters are required to describe the process related to the PS [16]. In contrast, although ABL is believed to be caused by the PS that naturally exist in fungal cells, whose types and amounts are usually unknown, first-principle modeling becomes even more challenging than modeling PDT.

Generally, to handle the challenges in modeling by first principles, system identification methods (SIM) that estimate models from the data measured from complex dynamic processes have been well developed in control theory literature [18]. In the recent decades, the applications of SIM methods to identify biological and biomedical systems, which are usually highly nonlinear, coupled and chaotic, have also been witnessed, e.g., in modeling arterial windkessel [19], aortic pressure [20] and electrodermal activity [21]. To deal with the nonlinearities in biological systems, various structured nonlinear dynamic model identification methods have been investigated, e.g., Wiener model [20] and NARMAX model [22].

Despite all the aforementioned efforts in biomedical system identification, identifying a nonlinear dynamic model for anti-fungal blue light therapy has not yet been targeted in the literature. However, some attempts have been made to handle similar problems. For instance, a closed-loop control scheme has been implemented to track the photobleaching trajectory during PDTs in [23], which is an ON/OFF controller designed without any model. A data-driven modeling method has been investigated in [24], which basically approximates the nonlinear PDT dynamics by a linear integrator model. Until now, no nonlinear model based on experimental data has been established. Furthermore, no study has analyzed the effects and safety of ABL therapy based on a dynamic ROS model.

In this study, ROS levels were measured in *C. albicans* and V. E. cells under irradiation from three LED light sources of different wavelengths, including 385, 405, and 415 nm. Then, these experimental data were fitted using a popular kernel-based method [25], e.g., nonlinear autoregressive with exogenous inputs (NARX) modeling [26], [27]. The advantage of using kernel based learning is mainly the treatment of the nonlinearity of a complex dynamic process by linearly combining a set of kernels. Furthermore, sparse kernel modeling can be applied to select the best kernel centers from the training samples. One popular approach is based on random selection by minimizing some cost functions, e.g., using the repeating weighted boosting search (RWBS) algorithm [28], which is an evolutionary algorithm based on weight boosting search. In this method, the kernel parameters and the centers are chosen by minimizing a MSE objective function. However, to search one regressor, it needs to be repeated for multiple times with initial random sampling, before finally converges to the global optimum. This iteration may reduce the algorithm efficiency. To avoid this iteration and

hence improve the efficiency, we choose the particle swarm optimization (PSO) algorithm instead of RWBS, which is a proven method for its fast searching speed [29]. The fitting accuracy of the NARX model to ROS detected in *C. albicans* and V. E. cells was satisfactory.

The contributions of the current study are three-fold. First, we conducted blue light stimulation experiments and measured the induced ROS in both *C. albicans* and V. E. cells, in response to three different wavelengths (385, 405, and 415 nm). Second, a kernel-based NARX model was developed and applied to the experimental data. Moreover, a new PSO-based kernel selection algorithm was proposed and applied to improve this NARX model. The fitting accuracy demonstrated the effectiveness of the modeling approach. Third, we analyzed the optimal ABL wavelength for treating VVC using the simulation results.

II. METHODS

A. NARX Modeling

The "kernel trick" was used to reduce the experimental burden and treat the nonlinearity of the dynamics of ROS accumulation, e.g., using the NARX model with a suitable kernel function. A general discrete-time nonlinear system is described as:

$$\boldsymbol{y}_k = f(\boldsymbol{y}_{k-1}, \ldots, \boldsymbol{y}_{k-n_y}, \boldsymbol{u}_{k-1}, \ldots, \boldsymbol{u}_{k-n_u}) + \boldsymbol{\epsilon}_k, \quad (1)$$

where $\boldsymbol{u}_k \in \mathbb{R}^m, \boldsymbol{y}_k \in \mathbb{R}^\ell$, and $\boldsymbol{\epsilon}_k \in \mathbb{R}^\ell$ are respectively the input, output, and noise vector at time instant k; $f(\cdot)$ is a nonlinear function; and $n_y, n_u \in \mathbb{N}$ represent respectively the output and input delays, e.g., $\boldsymbol{u}_{k-n_u} = \boldsymbol{u}_k \cdot z^{-n_u}$, with z^{-1} standing for the one step delay operator. The noise $\boldsymbol{\epsilon}_k$ is zero-mean white Gaussian with a covariance matrix Σ, i.e., $\boldsymbol{\epsilon}_k \sim \mathcal{N}(0, \Sigma)$.

To model the changes in intracellular ROS concentrations by (1), let $\boldsymbol{y}_k$ denote the ROS concentration at the kth time sampling point, f denote the ROS generation process, $\hat{\boldsymbol{y}}_k$ denote the estimated value of $\boldsymbol{y}_k$, and u_k denote the irradiance of the light. In ABL, the irradiance is usually kept constant during the entire treatment process, i.e., $u_k \equiv u, \forall k > 0$. So in (1), it is not necessary to consider the inputs at different delay steps. Instead, the effect of the exogenous input u can be considered as a step response. That is, when the light is switched on, the excitation of the ROS starts. Mathematically, this process can be rewritten as:

$$\boldsymbol{y}_k = \hat{\boldsymbol{y}}_k + \boldsymbol{\epsilon}_k = \tilde{f}_u(\boldsymbol{y}_{k-1}, \ldots, \boldsymbol{y}_{k-n_y}) + \boldsymbol{\epsilon}_k, \quad (2)$$

where $\tilde{f}_u(.)$ is defined as:

$$\tilde{f}_u(\boldsymbol{y}_{k-1}, \ldots, \boldsymbol{y}_{k-n_y}) = \begin{cases} 0, & \text{if } u_k = 0 \\ f(\boldsymbol{y}_{k-1}, \ldots, \boldsymbol{y}_{k-n_y}), & \text{if } u_k = u \end{cases}. \quad (3)$$

For simplicity, collect the sequence of $\boldsymbol{y}_{k-1}, \ldots, \boldsymbol{y}_{k-n_y}$ into a column vector, and denote it as $\boldsymbol{x}_k = [\boldsymbol{y}_{k-1}^T, \ldots, \boldsymbol{y}_{k-n_y}^T]^T$. Let the number of kernel basis functions be n. (2) was changed into the following regression model using some suitable functions that approximate $f(\cdot)$ with arbitrary accuracy,

$$\hat{\boldsymbol{y}}_k = \Sigma_{i=1}^n \boldsymbol{w}_i g_i(\boldsymbol{x}_k) \quad (4)$$

TABLE I
SOME POPULAR KERNEL FUNCTIONS, WITH $\boldsymbol{x}_i$ BEING THE CENTER AND $a_i, b_i,$ AND c_i BEING THE PARAMETERS OF THE i-TH KERNEL

Kernel	$g_i(\boldsymbol{x})$
Linear	$a_i \boldsymbol{x}^T \boldsymbol{x}_i + b_i$
polynomial	$(a_i \boldsymbol{x}^T \boldsymbol{x}_i + b_i)^{c_i}, a_i > 0, c_i \in \mathbb{N}^+$
Gaussian(RBF)	$exp\left(-\frac{\|\boldsymbol{x}-\boldsymbol{x}_i\|_2^2}{2a_i^2}\right)$
Laplace	$exp\left(-a_i\|\boldsymbol{x}-\boldsymbol{x}_i\|\right)$

where $\boldsymbol{w}_i \in \mathbb{R}^\ell, i = 1,\ldots,n$ are the corresponding weighting vectors; and $g_i, \in \mathbb{R}, i = 1,\ldots,n$, is a kernel function chosen from the popular candidates listed in Table I.

The number of I/O data samples was denoted by N. The output vectors were collected into a matrix as:

$$\boldsymbol{y} = \begin{bmatrix} \boldsymbol{y}_1 & \boldsymbol{y}_2 & \boldsymbol{y}_3 & \cdots & \boldsymbol{y}_N \end{bmatrix}^T \in \mathbb{R}^{N \times \ell} \qquad (5)$$

Similarly, the outputs of the kernel functions excited by $\boldsymbol{x}_1,\ldots,\boldsymbol{x}_N$ were collected into the following regressor matrix

$$\boldsymbol{G} = \begin{bmatrix} g_1(\boldsymbol{x}_1) & \ldots & g_n(\boldsymbol{x}_1) \\ \vdots & & \vdots \\ g_1(\boldsymbol{x}_N) & \ldots & g_n(\boldsymbol{x}_N) \end{bmatrix} \in \mathbb{R}^{N \times n}$$
$$= \begin{bmatrix} \boldsymbol{g}_1 & \boldsymbol{g}_2 & \boldsymbol{g}_3 & \cdots & \boldsymbol{g}_n \end{bmatrix}, \qquad (6)$$

where $\boldsymbol{g}_i = [g_i(\boldsymbol{x}_1), \ldots, g_i(\boldsymbol{x}_N)]^T$.

With the aforementioned definition, (4) can be written in compact form as

$$\boldsymbol{y} = \boldsymbol{G}\boldsymbol{w}, \qquad (7)$$

where $\boldsymbol{w} = [\boldsymbol{w}_1 \ \boldsymbol{w}_2 \ \boldsymbol{w}_3 \ \ldots \ \boldsymbol{w}_n]^T \in \mathbb{R}^{n \times \ell}$.

With a given regressor matrix, the only parameter in (7) to be estimated is the weight matrix $\boldsymbol{w}$. On the other hand, the regressor matrix is determined by the kernels with the set of parameters $\{\boldsymbol{x}_i, a_i, b_i, c_i, i = 1,\ldots,N\}$. The method to determine these kernels will be detailed later in what follows.

First, to solve $\boldsymbol{w}$, we use the QR factorization of $\boldsymbol{G}$, i.e.,

$$\boldsymbol{G} = \boldsymbol{P}\boldsymbol{A}, \qquad (8)$$

where $\boldsymbol{A} \in \mathbb{R}^{n \times n}$ is an upper diagonal matrix; $\boldsymbol{P} \in \mathbb{R}^{N \times n}$ is as orthogonal matrix. Therefore, (7) can be rewritten as

$$\boldsymbol{y} = \boldsymbol{G} \cdot \boldsymbol{w}$$
$$= \boldsymbol{P}\boldsymbol{A} \cdot \boldsymbol{w}$$
$$= \boldsymbol{P} \cdot \boldsymbol{\theta} \qquad (9)$$

where $\boldsymbol{\theta} = \boldsymbol{A}\boldsymbol{w} \in \mathbb{R}^{n \times \ell}$, and can simply be solved as $\boldsymbol{\theta} = \boldsymbol{P}^T \boldsymbol{y}$.

Learning a NARX model from data requires estimating the weights $\boldsymbol{\theta}$ and the parameters of the kernel functions, e.g., the kernel center $\boldsymbol{x}_i$. In this study, a kernel selection method based on particle swarm optimization (PSO) was applied to select a subset of the best kernels from the full set of candidate kernels. This selection algorithm is detailed in the Appendix

TABLE II
THE LEDs USED AND THEIR MAIN PARAMETERS, WHERE FWHM REPRESENTS FULL WIDTH AT HALF MAXIMUM

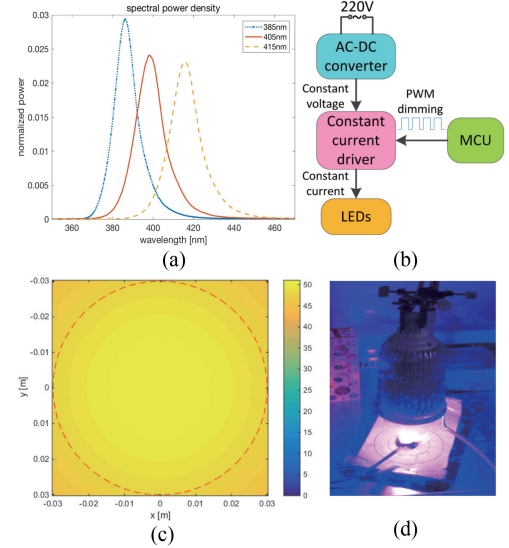| type	wavelength	FWHM
Vishay VLMU3500-385-120	385nm	10nm
Kingbright ATDS3534UV405B	405nm	15nm
LUMILEDS LUXEON LHUV-0415-A070	415nm	13.7mn

Fig. 1. LED light source design: (a) normalized SPD of the four types of LEDs, (b) electrical scheme, (c) simulated irradiance distribution, (d) photo of the experimental setup.

A. Incorporated by this selection algorithm, the entire NARX model identification algorithm is summarized in Appendix B.[1]

B. LED Light Source

Three different types of LEDs with the specified peak wavelengths respectively at 385 nm, 405 nm, and 415 nm were applied in this work. The types of these LEDs and their main parameters are listed in Table II. Their spectral power density (SPD) curves, as measured by a Maya2000Pro spectrometer (Ocean Optics, US), are depicted in Fig. 1(a). In this figure, every SPD curve is normalized with respect to its integral over the range of the measured wavelength, i.e., with each normalized SPD curve integrating to 1.

The LED light sources were designed following the procedures in [30], and were driven by a constant current source with PWM current level control to stabilize the output irradiance [31]. The LED chips are arranged in a 1.5cm-by-1.5 cm square as a 4-by-4 array. The three LED light sources can deliver an irradiance of $50\,mW/cm^2$ uniformly within a $60\,cm$-diameter circle. Fig. 1(c) shows the simulated irradiance distribution, where the average irradiance in the 6cm-diameter circle is $49.39\,mW/cm^2$, with a relative variation of only 6.56%. The

---

[1]The codes implementing these algorithms are available from https://drive.google.com/drive/folders/1tSwPW5aBiS3KYAWcTKwRapLasZ2ZqdSD?usp=sharing, or by contacting with the author.

irradiance was measured and confirmed by a PM100D power meter with a S120VC probe (Thorlabs, US). The schematic diagram of the electrical drive and control system and the experimental setup are illustrated in Figs. 1(b) and 1(d).

C. Culture Conditions for C. Albicans and the V. E. Cells

The human host cell line used in this study was the vaginal epithelial cell strain (VK2/E6E7 ATCC CRL-2616, ATCC, Manassas, VA, USA). The cell line was incubated in Dulbecco's modified Eagle's medium (Gibco, Carlsbad, CA, USA) supplemented with 10% fetal bovine serum at 37°C in a humidified atmosphere with 5% CO_2.

The *C. albicans* used in this study was the 3147 (IFO 1594) strain (ATCC). The fungal strain was cultured in tryptic soy broth at 26°C. To maintain the concentration of the fungal suspension within the same range, the absorption of the suspension was measured at 550 nm using the U-3900H spectrophotometer (Hitachi, Tokyo, Japan) before all experiments. The absorption levels measured by this equipment were always controlled in the range of 2.3-2.5, which corresponded to a fungi density of 10^7 CFU/ml.

D. ROS Assay

The fungi were centrifuged, separated from the medium, and dissolved in a 1,000-fold dilution of the ROS fluorescent probe (DCFH-DA assay kit, Beyotime Institute of Biotechnology, Beijing, China) in phosphate buffered saline. After incubating the suspension at $37^{o}C$ in a shaker for 30 min, the suspension was centrifuged three times to remove the redundant probe. Then, the suspension was seeded into a 96-well plate and was irradiated with one of the three LED light sources.

During the experiment, the cell suspension in one well was resuspended and taken out of the plate consecutively at 0, 5, 10, 15, 20, 25, and 30 min. The removed suspension in one well was placed in the dark; while the rest wells were kept under the irradiation of the light. Therefore, the fluence received by each well was 0, 15, 30, 45, 60, 75, and 90 J/cm^2, respectively, considering the light irradiance of 50 mW/cm^2. The intracellular ROS level of the cell suspension was measured immediately after the light treatment using a VL0L0TD0 Varioskan LUX microplate reader (Thermo Fisher, Waltham, MA, USA), with excitation and emitting wavelengths of 488 and 525 nm, respectively.

Finally, a sequence of ROS fluorescent levels up to 30 min were obtained. The entire experimental method was repeated three times independently. In total, triplicate experiments were performed. In each repeating experiment, a new cell strain was thawed and incubated, then seeded into a new 96-well plate, and finally irradiated following the aforementioned procedures.

E. Modeling the Viability of C. Albicans and V. E. Cells

Although the light-induced ROS causes cytotoxicity, the susceptibility to the ROS of the two cells can still be different, in the sense that the same amount of ROS may cause different viability reduction in both types of cells. To further investigate this issue,

the survival rates of *C. albicans* and V. E. cells affected by ABL were modeled.

The viability models take the following form, which is a piecewise function [13], [32], including a shoulder at the beginning of the ABL to represent the accumulating process of the light-induced cytotoxic ROS.

$$N_{c,e}(t) = \left\{ \begin{array}{ll} N_{c,e}(0), & t < \tau \\ N_{c,e}(0) \cdot e^{-\kappa(t-\tau)}, & t \geq \tau \end{array} \right., \qquad (10)$$

where $N_{c,e}(t)$ is the survival rate at time t; the subscripts "c, e" respectively represent the *C. albicans* and V. E. cells; κ is the decaying rate coefficient; and τ is the time constant of when the inactivation starts.

F. Statistics

In the ROS assays, the raw data were processed to produce the mean and standard deviation for each treatment time interval. The significance of ROS levels and viability of cells were tested by the Student's t-test. The values of $P < 0.05$ were considered statistically significant.

III. RESULTS

A. Measurements of the ROS Concentrations in C. Albicans and V. E. Cells During ABL Irradiation

The time sequences of the ROS concentrations in the *C. albicans* and V. E. cells were measured using all three light sources. The measured fluorescence levels were processed as $y = \frac{R}{R_0}$, where R_0 is the initial ROS fluorescence of the cells, i.e., the ROS level not altered by light, as the control group; R is the measured ROS fluorescence level after the ABL irradiation, as the treatment group; and y is the processed relative fluorescence level. We denoted the relative change in the *C. albicans* ROS level as y_c; and similarly denoted that of V. E. cells as y_e. The y_c and y_e values irradiated by ABL of the three wavelengths from 0 to 30 min are plotted in Fig. 2.

After *C. albicans* was exposed to light for 5 min, the relative ROS concentration y_c increased significantly in all cases (P<0.05); y_c increased 10-12 times within 30 min. The y_e value of the V. E. cells increased significantly after 5 min of light exposure in all cases (P<0.05); y_e was increased 3-6 times within 30 min. Considering the experimental data from the both cells together, y_c was significantly higher than y_e after 15 min of irradiation in all cases (P<0.05).

B. NARX Modeling and Comparison Between PSO and RWBS Kernel Selection Methods

The NARX was used to predict the dynamic changes in *C. albicans* ROS concentrations; and the data from the experiments with different wavelengths were fitted. The relative ROS concentration of *C. albicans* at the kth time sampling point was denoted by $y_c(k)$. Here, k is from 1 to 7; and corresponded *C. albicans* was irradiated for 0 to 30 min with a step size of 5 min. Let $n_y = 2$, i.e., in a second order nonlinear dynamic form. Then,
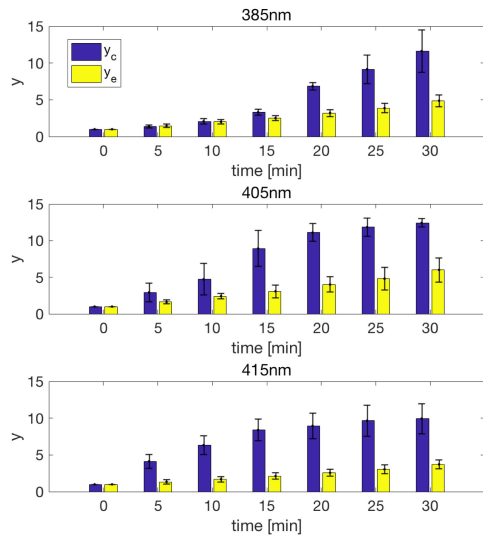
Fig. 2. Rrelative ROS levels of *C. albicans* and V. E. cells under irradiation with three wavelengths of ABL.

TABLE III
COMPARISON OF THE EFFICACY AND ACCURACY OF DIFFERENT KERNEL
SELECTION ALGORITHMS OF NARX MODEL

Selection algorithm	RMSE	Time cost (s)
RWBS	0.5642	2.747
PSO	0.5407	0.8364

the NARX model can be written as:

$$y_c(k) = \tilde{f}_u(y_c(k-2), y_c(k-1)) \qquad (11)$$

The ROS concentrations of the cells irradiated by 385, 405, and 415 nm wavelength light were measured as time-series data. These time-series data were used to estimate the NARX model. More specifically, seven data sampling points were processed with a delay of two steps to generate five pairs of I/O data as required in (11).

The NARX model was estimated as described in Section II-A using these five pairs of I/O data. Then, the first two data sampling points were taken to predict the third point. After that, the iteration was continued by plugging the predicted points into the right hand side of (11).

Here, we compared the kernel selection methods respectively by the PSO and RWBS algorithm [28], on fitting the NARX model to the data from the ABL experiment on the *C. albicans* under the irradiation of the 415 nm light. The parameters of RWBS algorithm were chosen the same as those used in [28], i.e., population size $Q = 40$, outer loop repeat times $N = 7$, and inner loop repeat times $K = 600$. The PSO parameters were $Q = 40$, $N = 1$ and $K = 5$, which can yield comparable model accuracy as the RWBS algorithm, as listed in Table III. The weighting factors of (12) in Appendix A were set to $d_1 = 0.6, d_2 = 0.6, d_3 = 0.5$ empirically.

For this problem, the average time cost of running the RWBS algorithm was about 2.7 seconds; while the average time cost

TABLE IV
COMPARISON OF THE ACCURACY OF THE NARX MODELS WITH DIFFERENT
KERNELS FITTED TO THE DATA FROM THE EXPERIMENTS WITH DIFFERENT
WAVELENGTHS

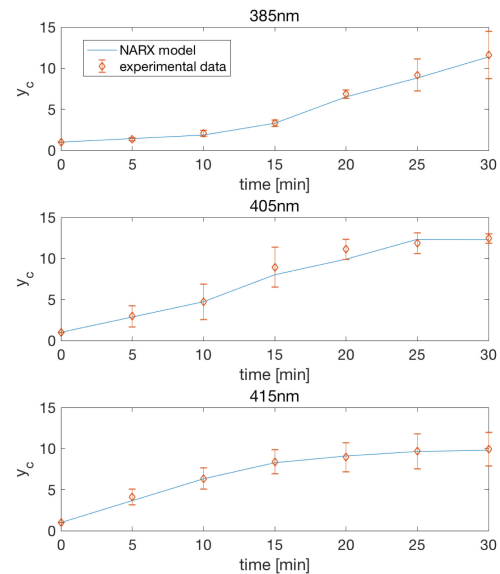| Wavelength [nm]	RMSE with different kernels			
	RBF	Laplace	Linear	Polynomial
385	0.8676	0.2019	0.8662	0.6051
405	0.7319	0.3163	0.9407	0.5748
415	0.2108	0.2931	0.2393	0.2394
Average	0.6035	0.2704	0.6821	0.4731

Fig. 3. The NARX model predicting the measured relative ROS concentrations in *C. albicans* from the 385, 405 and 415 nm light irradiation experiment, respectively.

of the PSO algorithm was only about 0.8 seconds. Both of them ended up with 2 best kernels.

C. NARX Modeling Based on C. Albicans ROS

To select a best kernel for $g_i(x)$ from the candidates listed in Table I, the NARX models were compared in simulations. They were compared in terms of the fitting error of the RMSEs of NARX models, which are shown in Table IV.

Since the Laplace kernel performs the best in the simulation, we chose the NARX model with the Laplace kernel to model the process in the following. This predicting results of the NARX model are shown in Fig. 3.

D. NARX Modeling Based on Measured ROS in V. E. Cells

Similar to Section III-C, the NARX model was used to predict the dynamic changes in the ROS concentrations of V. E. cells. The NARX model took the form of (11). As the increase in y_e was similar to that of y_c, we chose NARX with the Laplace kernel to model the process. The modeling accuracy of the NARX models against the data collected from different wavelengths is listed in Table V and plotted in Fig. 4.

TABLE V
THE RMSEs OF THE NARX MODEL WITH THE LAPLACE KERNEL
ESTIMATED BY THE EXPERIMENTAL DATA FROM V. E. CELLS

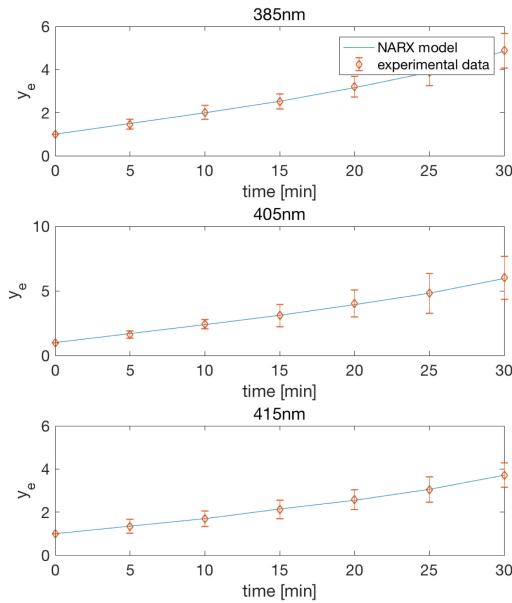| Wavelength	385nm	405nm	415nm	Average
RMSE	0.0544	0.0827	0.0409	0.0593

Fig. 4. The NARX model predicting the measured relative ROS concentrations in V. E. cells from the 385, 405 and 415 nm light irradiation experiment, respectively.

E. Analyzing the Safety and Efficacy of ABL Therapies via NARX Models

In the above sections, NARX models were established to estimate the ROS concentrations induced by single-wavelength ABL for *C. albicans* and V. E. cells. In this section, the ROS concentrations in the cells were compared using different NARX models. More specifically, we plotted the tuple of (y_c, y_e) stimulated by the same fluence ranging from 0 to 90 J/cm^2 with a step size of 15 J/cm^2. Here, fluence was calculated as the product of irradiance and irradiation time. The results are shown in Fig. 5. A dash line $y_c = y_e$ was plotted to better reflect the trends in the figure. It can be clearly observed that the ROS generation was greater in the *C. albicans* than in the V. E. cells for each wavelength and at a same amount of fluence. As shown in Fig. 5, the red dash curve (415 nm) is the lowest one among the three curves, which indicates the consistently lowest ROS generation in the V. E. cells under the 415 nm light exposure. Therefore, the 415 nm light had less damage to the human host cells than the 385 nm and 405 nm. In comparison, the 405 nm light was the most harmful to the V. E. cells.

F. Comparison of the NARX Models With Linear AR Models in Fitting the Experimental Data

To further show the advantage of the nonlinear NARX modeling approach, linear autoregressive (AR) models (see [18]) were also identified to predict the dynamic changes of ROS in the *C.*
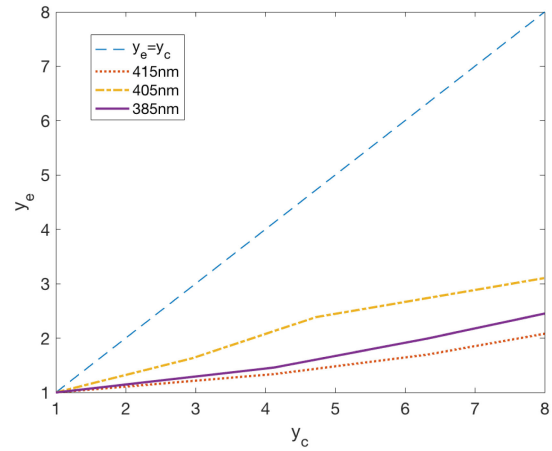

Fig. 5. Comparing the light-induced ROS concentration using the NARX models identified from the data of two types of cells.

TABLE VI
THE ACCURACY OF THE AR MODEL FITTED TO DATA OF ALL THE
THREE WAVELENGTHS

Wavelength [nm]	C. A.	V. E.
385	3.6702	0.9402
405	3.2734	1.6248
415	2.1904	1.3077
Average	3.0477	1.2909

TABLE VII
THE ACCURACY OF THE ESTIMATED NARX MODELS FITTED TO DATA OF
ALL THE THREE WAVELENGTHS. THE EXPERIMENTAL DATA USED WERE THE
C. ALBICANS TIME-SERIES ROS CONCENTRATIONS

Wavelength [nm]	Average RMSE with different kernels			
	RBF	Laplace	Linear	Polynomial
385	1.3707	1.1629	2.1573	0.9875
405	1.8357	2.8710	2.0509	0.9402
415	1.5546	1.1629	1.6395	1.5785

albicans and V. E. cells. Similar to the NARX model, the delay step was also set to 2. The RMSEs of the AR models are listed in Table VI. Clearly, the accuracy of the AR models was much lower than that of the NARX models with the Laplace kernels, which have been reported in Tables IV and V, respectively for *C. albicans* and V. E. cells.

G. Generalized NARX Model for Short Wavelength ABL Therapy

In this section, we developed a generalized NARX model to fit the experimental data from all three wavelengths. Here, the NARX model identified by the experimental data with one wavelength was used to fit the experimental data to all three wavelengths. The average fitting RMSEs of the NARX to the *C. albicans* experimental data are listed in Table VII. The NARX with a polynomial kernel estimated by 385 and 405 nm data performed well with a good generalized capability. Similarly, the polynomial kernel also showed good generalized capability

TABLE VIII
FITTED PARAMETERS OF THE VIABILITY MODEL (10)

	405nm		415nm	
	τ	κ	τ	κ
C. A.	769	85.9	450	3.80e-3
V. E.	56	224.3	526	5.81e-4

TABLE IX
ESTIMATED LETHAL DOSES, LD50 AND LD90, RESPECTIVELY FOR 50%
AND 90% VIABILITY REDUCTION

	405nm	415nm
LD50 $[J/cm^2]$	87.1	85.9
LD90 $[J/cm^2]$	282.5	224.3

for the V. E. cells data. The NARX model estimated by the 405 nm wavelength data performed the best of all.

H. The Survival Rates of C. Albicans and V. E. Cells Affected by ABL

By the aforementioned observations from Fig. 5, the 415 nm was the best choice for treating *C. albicans* infected VVC; while the 405 nm was the worst. Therefore, we only need to take these two extreme cases to study the inactivating effects on both *C. albicans* and V. E. cells. It shall be emphasized that since the main contribution of this work is to develop and verify the kernel-based NARX models of light-induced ROS concentrations, extensively repeating the well-studied viability assays is out of its scope. On the other hand, in our previous work [13], such experiments with exactly the same types of cells and experimental settings were already performed, which had resulted in the viability data, i.e., $N_c(t)$ and $N_e(t)$ for $t = 0, 5, 15, 20, 25$ min, from respectively the 405 nm and 415 nm light irradiation. The details of the applied materials and methods can be found therein.

(10) was fitted to these viability data, and applied to estimate the lethal doses of the V. E. cells. The fitted parameters are listed in Table VIII, with which the lethal doses of the V. E. cells were finally estimated, and are listed in Table IX. Note that calculating LD90 of the V. E. cells is especially relevant, because at the max fluence applied to the *C. albicans*, i.e., after the irradiation by either of the wavelengths for 25 min, N_c reached the order of 10^{-3}. However, at the same dosage, the survival rates of the V. E. cells were still a bit higher than 0.5, by either the 405 nm or 415 nm light. Since the treatment target had already been achieved, it was not necessary to further apply higher fluence to the V. E. cells. Therefore, the LD90 calculated by the model is a reasonable estimate of the dosage for killing up to 90% V. E. cells.

Furthermore, the tuples of (N_c, N_e) caused by the same dosages are illustrated in Fig. 6. Besides, linear lines were fitted to show the descending trends of the V. E. cells, as the viability rates of the *C. albicans* decreased. The slopes of the linear lines were -0.4733 and -0.4031, as respectively fitted to the experimental data of the 405 nm and 415 nm.
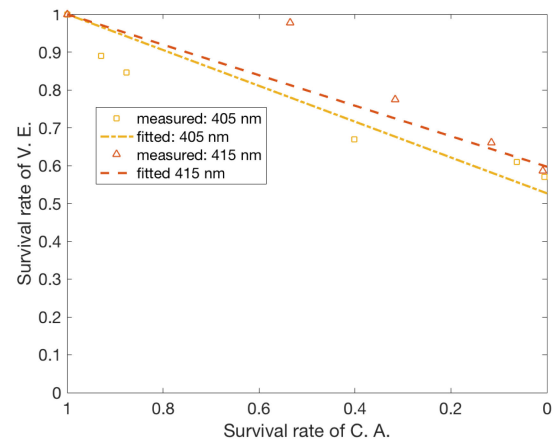

Fig. 6. The survival rates for the *C. albicans* and V. E. cell in the irradiation of three wavelengths, i.e., 385, 405, and 415 nm.

IV. DISCUSSION

A. Experimental and Simulation Results

In this study, the ROS generated during anti-fungal light irradiation experiments were measured with three different wavelengths. The main objectives were to compare the effects of the three different wavelengths on inducing ROS, and to build a NARX model to predict the changes in ROS levels.

In our experiments, light-induced ROS increased significantly in *C. albicans*, demonstrating the effectiveness of the ABL therapy. On the other hand, the ROS in the V. E. cells was also increased during blue light irradiation. However, the increased ROS ratio of V. E. cells was much lower than that of *C. albicans*, which demonstrates the safety of ABL therapy.

The ROS level produced by the 405 nm light was slightly higher than that of the other two wavelengths, indicating a higher effectiveness for inducing ROS in *C. albicans*. This coincided with the finding that the main PS in *C. albicans* is porphyrins [12], [33], whose peak absorption wavelength is 405 nm. Thus, the 405 nm blue light excited the porphyrins more effectively than the other two wavelengths.

V. E. cells were also most affected by the 405 nm blue light. Although the main endogenous PS in V. E. cells is flavin adenine dinucleotide, whose peak absorption wavelength is about 450 nm [34], they also include considerable coproporphyrin content [14]. Besides, the molar extinction coefficient of coproporphyrin is about 45 times higher than that of flavin adenine dinucleotide [35], [36]. Thus, 405 nm light also induced the ROS effectively in V. E. cells.

The main difficulty with ROS assay experiments is that the initial cellular ROS level is difficult to control. The initial cellular ROS level is proportional to the cell concentration, which is strictly controlled by absorption of the fungal suspension. Also, the culture conditions, e.g., media and passage or culture time, can affect the amount of cellular PS [37]; therefore, affecting the initial ROS level and ability of ROS to accumulate. In this study, the culture conditions were strictly controlled. All experiments were performed with fresh-thawed fungal strains, which were cultured for the same durations.

On the other hand, the performance of the polynomial kernel was best among the four kernels, when the generalized NARX model was used to fit the experimental data of all three wavelengths. The fitting accuracy of the linear kernel was not satisfactory, which was attributed to the nonlinearity of the ROS accumulation process. For instance, some kinetic models of light-induced ROS have been investigated [38]–[40] and all of these kinetic models demonstrated high nonlinearity.

In Section III-G, a generalized NARX model was developed to predict the ROS induced by the three wavelengths of light. In fact, the 385, 405 and 415 nm wavelengths include almost all of the short wavelength blue light. Thus, this generalized NARX model was useful to predict the ROS concentration with any short wavelength blue light. We did not perform experiments with long wavelength ABL, since it does not inactivate fungal strains [13], [34]. Thus, short wavelength ABL is a potential and effective treatment; and our generalized NARX model has provided a satisfactory prediction of the light-induced ROS concentration in responses to short wavelength blue light.

B. Comparison of the Effects Based on the Experimental and Simulation Results of All Three Wavelengths

The ROS concentrations in the different cells were compared in Section III-E. The dash line in Fig. 5 represents $y_c = y_e$, indicating the same ROS concentrations in *C. albicans* and V. E. cells in response to the same fluence of light. All three curves were always below it, which explains why the relative increase of ROS in V. E. cells was lower than that of *C. albicans*. More specifically, by the same relative ROS concentrations in *C. albicans* (y_c=8), the increase in the ROS ratio in V. E. cells was 2.6, 3, and 2.13, respectively with the 385, 405, and 415 nm light. Obviously, the 415 nm light has a more effective anti-fungal function with less damage to the human host cells than 385 and 405 nm.

However, the same amount of ROS may still cause different viability reduction in different types of cells. The slopes of the fitted lines in Fig. 6 help to further investigate this issue, which turned out to be -0.4733 and -0.4031, as respectively fitted to the experimental data of the 405 nm and 415 nm reported in our previous work [13]. The slope reflects the resistance of the V. E. cells to the light relatively to that of the *C. albicans*. The lower its absolute value, the more resistant the host cells to the light than the pathogens. Therefore, Fig. 6 shows that the 415 nm light has a more effective anti-fungal function with less damage to the human host cells than the 405 nm. Putting the observations from both Fig. 5 and Fig. 6 together, it can be concluded that the 415 nm is the best wavelength to treat this disease, in terms of both the efficacy and safety.

Notably, the 405 nm ABL was the most effective wavelength to induce the ROS in *C. albicans* and V. E. cells. However, the 415 nm is the better wavelength for treating VVC. This result reminds us that we should not only focus on the ROS accumulation by pathogens, but pay attention to the damage

to host cells. The peak absorption of specific pathogens, such as *C. albicans*, is 405 nm, determined by the endogenous PSs. However, this is not to say that the 405 nm is always the best ABL wavelength to treat candida infections.

C. The Safety of ABL

Clinically applicable anti-fungal strategies shall selectively inactivate pathogenic fungi, while sparing the normal host cells and tissues. As a safety study of ABL, both the ROS accumulation and survival rates were investigated and compared in *C. albicans* and V. E. cells. The increased ROS concentration in the V. E. cells was much lower than that in the *C. albicans*, implying the favorable selectivity of the ABL. During the 415 nm light exposure, no significant inhibition of the V. E. cells was observed within the beginning 10 min; while 47% of the *C. albicans* was killed at that time. In the end, over 58% of the V. E. cells survived after the 415 nm light irradiation, which almost completely inactivated the *C. albicans*. The aforementioned results suggest that there exists a therapeutic window, where the *C. albicans* can be selectively inactivated, while the majority of V. E. cells are preserved.

Furthermore, the maximum ABL fluence applied in this study was $90 J/cm^2$. Such a fluence is a safe dose without causing any genotoxicity to human host cells. It has been reported by other authors that no ABL induced DNA damage occurred in the epithelial cells up to the $216 J/cm^2$ fluence of 405 nm light [14]. For the more sensitive human retinal pigment epithelial (RPE) cells, it has also been observed that the induced damage to the mitochondrial DNA in the RPE cells was less at the fluence of $60 J/cm^2$ than that at $30 J/cm^2$ [41]. This may be attributed to the DNA repair system that was activated after the $30 J/cm^2$ light treatment. In fact, it was proved that the mitochondria are capable of repairing oxidative DNA damage to some extent, e.g., the damage to bases and single-strand breaks [42].

V. CONCLUSION

In this study, we measured the changes in intracellular ROS of *C. albicans* and V. E. cells for 30 min with irradiation of 385, 405, and 415 nm light. Furthermore, we proposed a modeling scheme using a kernel-based NARX structure, whose kernels were selected by a newly developed algorithm based on PSO optimization. This NARX model was used to fit the experimental data. High fitting accuracy was achieved by the model, demonstrating the effectiveness of the proposed modeling technique. Both the experimental data and the numerical results from the NARX model indicated that the ROS ratio of V. E. cells was always lower than that of *C. albicans*, demonstrating the safety of the ABL therapy. Moreover, a key conclusion was that the 415 nm wavelength blue light was the most effective wavelength, with the least damage to V. E. cells. More importantly, the proposed kernel-based NARX model identification algorithm can also be applied to determine the effective and safe light dosages in treating other types of fungal infection diseases.

APPENDIX A
PSO ALGORITHM FOR KERNEL SELECTION

The PSO algorithm is an evolutionary algorithm that mimics the movements of the organisms in a bird flock. It solves a problem by having a population of candidate solutions, and moving these particles around in the search-space. The movements of the particles are guided by their own best known position in the search space as well as the best known position of the entire swarm.

First, all particles are dispersed uniformly. The movement, also known as velocity, is denoted as $\boldsymbol{V}$, whose initial value can be randomly chosen. Let $\boldsymbol{\Psi}_j, \boldsymbol{V}_j \in \mathbb{R}^S$ denotes the j-th particle and its corresponding velocity, where S denotes the dimension of $\boldsymbol{\Psi}_j$ and $\boldsymbol{V}_j$. The movements are adapted by the following formula.

$$\boldsymbol{V}_j = d_1 \boldsymbol{V}_j + d_2(\boldsymbol{\Psi}^* - \boldsymbol{\Psi}_j) + d_3(\boldsymbol{\Psi}_j^* - \boldsymbol{\Psi}_j), \quad (12)$$

where d_1, d_2 and d_3 are the weighting factors; $\boldsymbol{\Psi}^*$ and $\boldsymbol{\Psi}_{j*}$ are the global best particle and local best particle respectively. The value of $\boldsymbol{V}_j$ shall be hard bounded to the so-called "setting region," i.e. $\boldsymbol{V}_j \in [\boldsymbol{V}_{min}, \boldsymbol{V}_{max}]$.

After each movement, the position of the j-th particle is updated by

$$\boldsymbol{\Psi}_{j+1} = \boldsymbol{\Psi}_j + \boldsymbol{V}_j, \quad (13)$$

which is then hard bounded to the search space, i.e. $\boldsymbol{\Psi}_j \in [\boldsymbol{\Psi}_{min}, \boldsymbol{V}_{max}]$. The search will stop when the cost function of $\boldsymbol{\Psi}^*$ is satisfied or the maximum generation is reached.

In this work, we propose to use PSO for the kernel selection in the NARX model. The objective of kernel selection is to select a subset of n_s ($n_s \ll n$) best kernels from the full set of n candidate kernels. In this specific NARX model, the I/O data are time-series data of the ROS concentrations which is a vector. To model each this process, the output dimension is $\ell = 1$, and hence y_k, θ_i take the scalar form. For simplicity of notations, we will especially consider the single output case. However, it shall be mentioned that the proposed method is not restricted to single output case. For the NARX kernel selection, define a cost function as J_t, where t stands for the number of selected regressors. The initial cost is denoted as $J_0 = \boldsymbol{y}^T \boldsymbol{y}$. According to Eq. (8) one can write

$$J_0 = \boldsymbol{\theta}^T \boldsymbol{P}^T \boldsymbol{P} \boldsymbol{\theta} = \Sigma_{i=1}^n \boldsymbol{p}_i^T \boldsymbol{p}_i \theta_i^2.$$

The idea is to search all the columns in $\boldsymbol{P}$, and find the one that reduces the cost value most, if being removed from J.

$$J_i = J_{i-1} - \boldsymbol{p}_i^T \boldsymbol{p}_i \theta_i^2, \quad (14)$$

where $\boldsymbol{p}_i$ is chosen from $\boldsymbol{P}$. This procedure can be terminated if

$$J_i < \epsilon \ or \ i < T \quad (15)$$

is satisfied, where ϵ is a chosen positive scalar; and "T" is the maximum epoch, represents that T regressors are chosen.

The PSO algorithm is proposed to choose the orthogonal columns in (14). In PSO, the decision variables are regarded as particles. These particles move around in the search space.

The parameters in the NARX model to be optimized are the kernel center $\boldsymbol{x}_i$ and the kernel parameters $a_i, b_i, \ldots$. Thus, for kernel selection, the particle shall include the index of the center and its corresponding variance; i.e., $\boldsymbol{\Psi}_j = [i_j, a_{i_j}, b_{i_j}, \ldots]^T$, where i_j stands for the index of the kernel center that is included in the j-th particle while choosing $\boldsymbol{p}_i$. Once these kernel parameters are fixed, the corresponding $\boldsymbol{p}_i$ and θ_i can be calculated by the standard Gram-Schmidt procedure; and the cost function can be calculated by (14).

APPENDIX B
NARX MODEL IDENTIFICATION ALGORITHM

Outer loop (search the i-th regressor $\boldsymbol{g}_i$, $i = 1, 2, \ldots, T$)
Initialize the value of population size denoted as Q; the weighting factors d_1, d_2 and d_3; the searching space $\boldsymbol{\Psi}_{min}, \boldsymbol{\Psi}_{max}$; and the movement setting region $\boldsymbol{V}_{min}, \boldsymbol{V}_{max}$.
for (i=1; i $\leq$ T; i=i+1)
1) Initialize the population $\boldsymbol{\Psi}$ randomly in the searching space and randomly generate an initial velocity matrix $\boldsymbol{V}$ inside the setting region.
2) Calculate the cost for all particles:
for (j=1; j $\leq$ Q; j=j+1)
a) Choose the kernel index i_j from the particle $\boldsymbol{\Psi}_j = [i_j, a_{i_j}, b_{i_j}, \ldots]^T$. Compute the regressor vector $\boldsymbol{g}_{i_j} = [g_{i_j}(\boldsymbol{x}_1), \ldots, g_{i_j}(\boldsymbol{x}_N)]^T$ by the kernel functions on Table (II), as a candidate while selecting the i-th regressor. Then orthogonalize it by the standard Gram-Schmidt procedure:
b) if $i = 1$

$$\boldsymbol{u}_j = \boldsymbol{g}_{i_j}$$
$$\boldsymbol{p}_{i_j} = \frac{\boldsymbol{u}_j}{\|\boldsymbol{u}_j\|_2} \quad (16)$$

else

$$\boldsymbol{u}_j = \boldsymbol{g}_{i_j} - \Sigma_{r=1}^{i-1}(\boldsymbol{g}_{i_j}^T \cdot \boldsymbol{p}_r) \cdot \boldsymbol{p}_r \quad (17)$$

$$\boldsymbol{p}_{i_j} = \frac{\boldsymbol{u}_j}{\|\boldsymbol{u}_j\|_2}$$

c) Calculate the corresponding θ_{i_j} and the cost function in terms of $\boldsymbol{p}_{i_j}, \theta_{i_j}$ by

$$\theta_{i_j} = \frac{\boldsymbol{p}_{i_j}^T y}{\boldsymbol{p}_{i_j}^T \boldsymbol{p}_{i_j}} \quad (18)$$

$$J_{i_j} = J_{i_{j-1}} - \boldsymbol{p}_{i_j}^T \boldsymbol{p}_{i_j} \theta_{i_j}^2 \quad (19)$$

where J_{i_j} is the cost after choose $\boldsymbol{\Psi}_j = [i_j, a_{i_j}, b_{i_j}, \ldots]^T$ as the i-th regressor.
end for
3) Find the best particle, as the one corresponding to the minimal J_{i_j}, i.e.

$$j* = \min_j \{J_{i_1}, J_{i_2}, \ldots, J_{i_Q}\}.$$

And set the global best as $\boldsymbol{\Psi}^* = \boldsymbol{\Psi}_{j*}$.

4) Initialize the local best particles as

$$\Psi_{j*} = \Psi_j, j = 1, 2, \ldots, Q$$

The PSO inner loop:
for(k=1; k ≤ K; k=k+1)
    for($j = 1; j \leq Q, j = j + 1$)
a) Calculate V_j by (12) and restrict its value into the setting region.
b) Update Ψ_j by (13) and restrict its value into the search space.
c) Calculate the cost function value J_{i_j} as in (19) for the new particle. Update the global best particle Ψ^* and the local best particles Ψ_i^* as follows.
If Ψ_j is better than Ψ^*, set $\Psi^* = \Psi_j$.
If Ψ_j is better than Ψ_j^*, set $\Psi_j^* = \Psi_j$.
end for
Stop the inner loop when the maximum epoch is reached or $J_{i_j}^* < \epsilon$.
end for
End of inner loop

The best particle find in this epoch is Ψ^*. Set $J_i = J_{i_{j*}}$, $g_i = g_{i_{j*}}$, $p_i = p_{i_{j*}}$ and $\theta_i = \theta_{i_{j*}}$. Remove the selected index $j*$ from the candidates of the regressor indices.

    end for
End of outer loop

REFERENCES

[1] T. Arendorf and D. Walker, "The prevalence and intra-oral distribution of Candida albicans in man," *Arch. Oral Biol.*, vol. 25, no. 1, pp. 1–10, 1980.

[2] J. D. Sobel, "Vaginitis," *N. Engl. J. Med.*, vol. 337, no. 26, pp. 1896–1903, 1997.

[3] A. Erdogan and S. S. Rao, "Small intestinal fungal overgrowth," *Curr. Gastroenterol. Rep.*, vol. 17, no. 4, pp. 1–7, 2015.

[4] R. A. Calderone and W. A. Fonzi, "Virulence factors of Candida albicans," *Trends Microbiol.*, vol. 9, no. 7, pp. 327–335, 2001.

[5] J. D. Sobel, "Candidal vulvovaginitis," *Clin. Obstet. Gynecol.*, vol. 36, no. 1, pp. 153–165, 1993.

[6] R. Hurley and J. de Louvois, "Candida vaginitis," *Postgrad. Med. J.*, vol. 55, no. 647, pp. 645–647, 1979.

[7] F. C. Odds *et al.*, *Candida and Candidosis: A Review and Bibliography*. London, U.K.: Baillière Tindall, 1988.

[8] L. Ljung, System Identification: Theory for the User, 2nd Ed. Upper Saddle River, NJ, USA: Prentice Hall, 1999..

[9] P. Vandeputte *et al.*, "Antifungal resistance and new strategies to control fungal infections," *Int. J. Microbiol.*, vol. 2012, 2012, Art. no. 713687.

[10] T. Maisch, "A new strategy to destroy antibiotic resistant microorganisms: Antimicrobial photodynamic treatment," *Mini Rev. Med. Chem.*, vol. 9, no. 8, pp. 974–983, 2009.

[11] R. Yin *et al.*, "Light based anti-infectives: Ultraviolet C irradiation, photodynamic therapy, blue light, and beyond," *Curr. Opin. Pharmacol.*, vol. 13, no. 5, pp. 731–762, 2013.

[12] Y. Zhang *et al.*, "Antimicrobial blue light inactivation of Candida albicans: In vitro and in vivo studies," *Virulence*, vol. 7, no. 5, pp. 536–545, 2016.

[13] T. Wang *et al.*, "Blue light therapy to treat Candida vaginitis with comparisons of three wavelengths: An in vitro study," *Lasers Med. Sci.*, vol. 35, no. 6, pp. 1329–1339, 2020.

[14] Y. Wang *et al.*, "Photoinactivation of neisseria gonorrhoeae: A paradigm-changing approach for combating antibiotic-resistant gonococcal infection," *J. Infect. Dis.*, vol. 220, no. 5, pp. 873–881, 2019.

[15] K. Wang *et al.*, "A comprehensive mathematical model of microscopic dose deposition in photodynamic therapy," *Med. Phys.*, vol. 34, no. 1, pp. 282–293, 2007.

[16] M. Kim *et al.*, "On the in-vivo photochemical rate parameters for PDT reactive oxygen species modeling," *Phys. Med. Biol.*, vol. 62, no. 5, pp. R1–R48, 2017.

[17] T. Zhu *et al.*, "Macroscopic modeling of the singlet oxygen production during PDT," *Proc. SPIE*, vol. 6427, 2007, Art. no. 642708.

[18] L. Ljung, *System Identification - Theory for the User*, 2nd ed. Upper Saddle River, NJ, USA: Prentice-Hall, 1987.

[19] T. Kind *et al.*, "Estimation of three- and four-element windkessel parameters using subspace model identification," *IEEE. Trans. Biomed. Eng.*, vol. 57, no. 7, pp. 1531–1538, Jul. 2010.

[20] A. M. Patel *et al.*, "Aortic pressure estimation using blind identification approach on single input multiple output nonlinear Wiener systems," *IEEE. Trans. Biomed. Eng.*, vol. 65, no. 6, pp. 1193–1200, Jun. 2018.

[21] M. R. Amin and R. T. Faghih, "Sparse deconvolution of electrodermal activity via continuous-time system identification," *IEEE. Trans. Biomed. Eng.*, vol. 66, no. 9, pp. 2585–2595, Sep. 2019.

[22] Y. Gu *et al.*, "Nonlinear modeling of cortical responses to mechanical wrist perturbations using the NARMAX method," *IEEE. Trans. Biomed. Eng.*, vol. 68, no. 3, pp. 948–958, Mar. 2020.

[23] J. Tylcz *et al.*, "Realtime tracking of the photobleaching trajectory during photodynamic therapy," *IEEE. Trans. Biomed. Eng.*, vol. 64, no. 8, pp. 1742–1749, Aug. 2017.

[24] J. Dong and T. Wang, "Data driven modeling of the reactive oxygen species stimulated by photon energy in light therapies," *IEEE Access*, vol. 8, pp. 18196–18206, 2020.

[25] S. Chen, C. F. N. Cowan, and P. M. Grant, "Orthogonal least squares learning algorithm for radial basis function networks," *IEEE Trans. Neural Netw. Learn. Syst.*, vol. 2, no. 2, pp. 302–309, Mar. 1991.

[26] J. Dong, "Recursive NARX model identification of nonlinear chemical processes with matrix invertibility analysis," *Comput. Chem. Eng.*, vol. 121, pp. 574–583, 2019.

[27] W. Lee *et al.*, "NARX modeling for real-time optimization of air and gas compression systems in chemical processes," *Comput. Chem. Eng.*, vol. 115, pp. 262–274, 2018.

[28] S. Chen, X. X. Wang, and C. J. Harris, "NARX-based nonlinear system identification using orthogonal least squares basis hunting," *IEEE Trans. Contr. Syst. Technol.*, vol. 16, no. 1, pp. 78–84, Jan. 2008.

[29] C. Ou and W. Lin, "Comparison between PSO and GA for parameters optimization of PID controller," in *Proc. Int. Conf. Mechatronics Automat.*, 2006, pp. 2471–2475.

[30] J. Dong and Z. Zhang, "Design of LED light for stimulating cells in the study of light therapies," in *Proc. 15th China Int. Forum Solid State Lighting: Int. Forum Wide Bandgap Semicond. China*, 2018, pp. 1–4.

[31] J. Dong and D. Xiong, "Applications of light emitting diodes in health care," *Ann. Biomed. Eng.*, vol. 45, no. 11, pp. 2509–2523, 2017.

[32] R. Buchanan *et al.*, "Differentiation of the effects of pH and lactic or acetic acid concentration on the kinetics of listeria monocytogenes inactivation," *J. Food Protect.*, vol. 56, no. 6, pp. 474–478, 1993.

[33] V. Plavskii *et al.*, "Porphyrins and flavins as endogenous acceptors of optical radiation of blue spectral region determining photoinactivation of microbial cells," *J. Photochem. Photobiol. B: Biol.*, vol. 183, pp. 172–183, 2018.

[34] Y. Wang *et al.*, "Antimicrobial blue light inactivation of neisseria gonorrhoeae: Roles of wavelength, endogenous photosensitizer, oxygen, and reactive oxygen species," *Lasers Surg. Med.*, vol. 51, no. 9, pp. 815–823, 2019.

[35] C. Rimington, "Spectral-absorption coefficients of some porphyrins in the Soret-band region," *Biochem. J.*, vol. 75, no. 3, pp. 620–623, 1960.

[36] J. A. Lewis and J. C. Escalante-Semerena, "The FAD-dependent tricarballylate dehydrogenase (TcuA) enzyme of Salmonella enterica converts tricarballylate into cis-aconitate," *J. Bacteriol.*, vol. 188, no. 15, pp. 5479–5486, 2006.

[37] J. Fyrestam *et al.*, "Influence of culture conditions on porphyrin production in aggregatibacter actinomycetemcomitans and porphyromonas gingivalis," *Photodiagnosis Photodyn. Ther.*, vol. 17, pp. 115–123, 2017.

[38] N. Lopez *et al.*, "Tumor reactive ringlet oxygen approach for Monte Carlo modeling of photodynamic therapy dosimetry," *J. Photochem. Photobiol. B: Biol.*, vol. 160, pp. 383–391, 2016.

[39] G. Kareliotis *et al.*, "Assessment of singlet oxygen dosimetry concepts in photodynamic therapy through computational modeling," *Photodiagnosis Photodyn. Ther.*, vol. 21, pp. 224–233, 2018.

[40] K. Wang, "Explicit dosimetry for photodynamic therapy: Macroscopic singlet oxygen modeling," *J. Biophotonics*, vol. 3, no. 5/6, pp. 304–318, 2010.

[41] B. Godley *et al.*, "Blue light induces mitochondrial dna damage and free radical production in epithelial cells," *J. Biol. Chem.*, vol. 280, no. 22, pp. 21061–21066, 2005.

[42] V. A. Bohr and R. M. Anson, "Mitochondrial DNA repair pathways," *J. Bioenerg. Biomembr.*, vol. 31, no. 4, pp. 391–398, 1999.